NUCLEI SEGMENTATION OF FLUORESCENCE MICROSCOPY IMAGES BASED ON MIDPOINT ANALYSIS AND MARKED POINT PROCESS

Neeraj J. Gadgil[⋆] *Paul Salama*[†] *Kenneth W. Dunn*[‡] *Edward J. Delp*[⋆]

[⋆]Video and Image Processing Laboratory
School of Electrical and Computer Engineering
Purdue University
West Lafayette, Indiana

[†]Department of Electrical and
Computer Engineering
Indiana University-Purdue University
Indianapolis, Indiana

[‡]Division of Nephrology
School of Medicine
Indiana University
Indianapolis, Indiana

ABSTRACT

Microscope image analysis is challenging because of non-uniform brightness, decreasing image contrast with tissue depth, poor edge details and irregular and unknown structures. In this paper, we present a nuclei segmentation and counting method using midpoint analysis, shape-based function optimization and a MPP simulation with a spatial birth-death process. Preliminary results demonstrate efficacy of the proposed method.

***Index Terms*—** biomedical image segmentation, marked point process, fluorescence microscopy

I. INTRODUCTION

In recent years, optical microscopy has become a powerful technique in biomedical research. Multi-photon microscopy is capable of producing image volumes deep into biological tissues and thus characterizing large scale biological structures at subcellular resolution [1], [2], [3]. The size and complexity of these images volumes make manual approaches for visualization and analysis impractical. Image segmentation methods are required to obtain quantitative, objective and reproducible measurements [4]. Images collected using fluorescence microscopy present challenges for image segmentation. They are inherently anisotropic and contain various aberrations and distortions that vary in different axes [5] and increase with depth.

One of the recent image analysis techniques, the stochastic active contour scheme (STACS) that makes use of image textures, edge, and region-based information for image segmentation was proposed in [6]. A topology preserving variant of STACS, that combines topology with level set formulation, was developed in [7], and was shown to outperform the seeded watershed algorithm [8]. Another topologically consistent method was developed for segmentation of cell nuclei and cellular boundaries [9]. A method to separate clustered nuclei in cellular images using shape markers and marking function in a watershed-like algorithm was developed [10] which was shown to outperform the classical watershed [11] and marker-controlled watershed using condition erosion [12]. The active mask approach [13], a recent region based method, used the relative homogeneity of the statistical properties of the foreground and background. A spatially adaptive method based on local characteristics of nuclei boundary and a priori shape model was described to address the segmentation of overlapping nuclei [14]. Another model-based approach that models a human segmenting an image using attributed relational graphs was presented in [15]. A 3D nuclei segmentation method based on level set deformable models and convex optimization was developed in [16].

A marked point process (MPP) method that models objects using stochastic techniques was described in [17]. A stochastic simulation of MPP was used as a powerful image analysis approach in which geometric properties of an image are used as the prior distribution and image data are considered at the object level [18]. An application of MPP to detect small brain lesions using a reversible jump Markov chain Monte Carlo (RJMCMC) algorithm was described in [19]. A unified Markov random field (MRF) and MPP based method was developed in [20]. Simulating stochastic processes requires a large number of iterations and demands large computation resources [21]. To assign a value that represents likelihood of the object with a given configuration to each possible object orientation at each pixel and search in that high dimensional space is also computationally intensive. Many adaptive approaches have been developed to address these challenges.

This work was supported by a George M. O'Brien Award from the National Institutes of Health NIH/NIDDK P30 DK079312. The image data was provided by Malgorzata Kamocka of Indiana University and was collected at the Indiana Center for Biological Microscopy.

Our datasets consist of 3D volumes of the kidney collected using two-photon microscopy of rat kidneys labeled with Hoechst 33342 which labels cell nuclei. The blue channel of the images collected results from the fluorescence of this label. One of our goals is to count the number of nuclei per unit length and per unit volume in the image. It is also desired to quantify area/volume of each nucleus.

In this paper, we propose a nuclei segmentation method in which we use adaptive thresholding and midpoint analysis as pre-processing that classifies components such that the computationally expensive MPP is used only for some components and a relatively simpler shape-fitting method for the rest of the components. Our MPP method is based on the one used in [18]. In our implementation, we use ellipse as object model and a modified energy function to account for non-uniform brightness typically present in fluorescene microscopy images. Our proposed approach is intended to provide automatic segmentation of microscopy images with non-uniform brightness, consisting of multiple overlapping objects that can be modeled using specific geometric shapes.

II. OUR PROPOSED METHOD

As shown in Figure 1, we first extract the blue color channel from three channels of a stack of microscopy images that are obtained by imaging a biological entity using different focal planes. This is called original image stack $\mathcal{I}$. A 3D adaptive thresholding is employed on the $\mathcal{I}$ to get segmentation mask $\mathcal{S}_{Th}$. For each image, midpoints analysis is subsequently used to produce two distinct masks: Λ_S and Λ_M. A distance function optimization method is used with the first mask and a MPP based method is used with the second mask. Segmentation results of the two methods, Ω_S and Ω_M respectively, are combined to produce the final segmented image Ω.

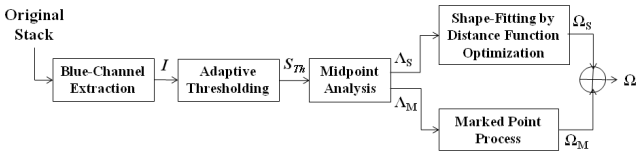

Fig. 1: Our proposed segmentation method.

Adaptive Thresholding: Our method employs initially an adaptive thresholding scheme. The objective of this step is to separate the foreground that represents the presence of a biological quantity in an image. This is done using two functions: a thresholding function f_{Th} that uses a 3D neighborhood information to assign signed and scaled value to each pixel and a voting function f_v that uses a Gaussian filter to aggregate weighted votes, similar to the voting-based distributing function used in [13].

Let $\mathcal{I}(t) \in [0,1]$ be the pixel intensity at pixel t of the original image stack $\mathcal{I}$. Let $(w_{Th,x} \times w_{Th,y} \times w_{Th,z})$ be the 3D window centered at pixel t and let τ_t be the mean pixel intensity of this window. The thresholding function $f_{Th} : [0,1] \rightarrow [-1,1]$ is used to assign to each

pixel t a linearly scaled value and a sign, based on its original intensity $\mathcal{I}(t)$ and the local mean τ_t, as indicated by Eq. 1.

$$f_{Th}(t) = \begin{cases} \frac{\mathcal{I}(t)-(\tau_t+\tau_c)}{1-(\tau_t+\tau_c)} & \text{if } \mathcal{I}(t) \geq (\tau_t+\tau_c) \\ -\frac{(\tau_t+\tau_c)-\mathcal{I}(t)}{(\tau_t+\tau_c)} & \text{if } \mathcal{I}(t) < (\tau_t+\tau_c) \end{cases} \quad (1)$$

where τ_c is a positive constant. Let $g_v(x,y,z)$ be a 3D truncated Gaussian function: $g_v(x,y,z) = e^{-\frac{|x|^2+|y|^2+|z|^2}{a^2}}$, where $x = -w_{v,x},..,0,..,w_{v,x}$, $y = -w_{v,y},..,0,..,w_{v,y}$ and $z = -w_{v,z},..,0,..,w_{v,z}$. The voting function $f_v(t) : [-1,1] \rightarrow [-\infty,\infty]$ is used to assign each pixel a value that is the summation of f_{Th} values from its neighborhood, weighted using $g_v(x,y,z)$:

$$f_v(t) = (f_{Th} * g_v)(t) \quad (2)$$

Now, based on the sign of $f_v(t)$, pixel t is segmented as foreground mask: $\mathcal{S}_{Th} = \{t : f_v(t) \geq 0\}$, where $\mathcal{S}_{Th}$ is the set of foreground pixels from volume $\mathcal{I}$. The outcome of this step: initial segmentation mask $\mathcal{S}_{Th}$ is used in the subsequent steps to do nuclei segmentation.

The constant threshold τ_c is selected empirically for a particular image stack based on the desired brightness of a segmented nuclei. A higher τ_c reflects segmenting fewer pixels with intensities being significantly above the local mean. $\tau_c \geq 0$ is necessary to avoid assigning regions with pixel intensities ≈ 0 as foreground.

Object Model: In order to count the number of nuclei and quantify their size in each image j, we use an ellipse as the shape model for objects to be segmented. The shape parameters for each elliptical object centered at (c) are the lengths of the semi-major and semi-minor axes (a,b) and the orientation angle of the semi-major axis with the horizontal (θ). Let $\rho = (a,b,\theta)$ be the parameter vector such that $\rho \in \mathcal{P}$, the parameter space. Based on the size of objects to be segmented, we limit the parameter space with $a \in (a_{\text{min}}, a_{\text{max}})$ $b \in (b_{\text{min}}, b_{\text{max}})$. Also, Δ_θ be the stepsize considered for angular orientations θ of an object.

Midpoint Analysis: Let $\mathcal{S}_{Th,j}$ be the segmentation mask for image I_j. Let λ be a connected component of $\mathcal{S}_{Th,j}$, using a 4-point neighborhood. Small components can be safely removed to preserve a high-level structural continuity. Therefore, λ in which the number of pixels is smaller than a threshold ν is not considered for midpoint analysis. The goal of midpoint analysis is to classify λs in $\mathcal{S}_{Th,j}$ into two groups: single-object components (Λ_S) and multiple-objects components (Λ_M). We first determine the potential midpoint locations/pixels by horizontally and vertically scanning the rows and column respectively, as shown in Figure 2 (a), using a process similar to the one described in [22]. This generates two sets of potential midpoints $\{m_{c,x}\}$ and $\{m_{c,y}\}$ along the rows and columns of the connected component λ, and which are depicted in blue and orange respectively, in Figure 2 (a). A pixel that is detected in both $\{m_{c,x}\}$ and $\{m_{c,y}\}$ is called as a midpoint pixel m_c as indicated by the pixel colored in red.

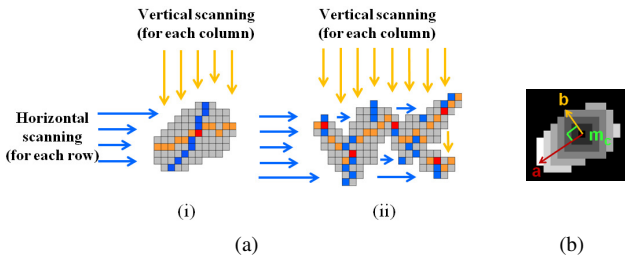

Fig. 2: Examples of midpoint analysis and selecting ellipse parameters for shape-fitting.

We assume that the components with one or no midpoint pixel m_c contain a maximum of one object and hence belong to Λ_S. Components containing more than one m_c may contain multiple objects and belong to Λ_M. Thus, $\Lambda_S = \{\lambda : \lambda \text{ contains at most one } m_c\}$ and $\Lambda_M = \{\lambda : \lambda \text{ contains more than one } m_c\text{'s}\}$, where $\Lambda_S \cap \Lambda_M = \phi$. An example component shown in Figure 2 (a)(i) belongs to Λ_S and that in Figure 2 (a)(ii) belongs to Λ_M.

Shape Fitting by Distance Function Optimization: We use a distance function to determine the parameters of the elliptical object for a $\lambda \in \Lambda_S$ in an image I_j. Let A_1 be an elliptical disk centered at s with parameters $\rho = (a,b,\theta)$. Let A_2 be the outer elliptical ring with parameters $(a+1, b+1, \theta)$. Using the empirical means and variances of the pixels belonging to A_1 and A_2 at pixel s with parameters ρ:

$\mu_1(s,\rho) = \frac{\sum_{u \in A_1} I_j(u)}{N_1}$, $\sigma_1{}^2(s,\rho) = \frac{\sum_{u \in A_1} I_j{}^2(u)}{N_1} - \mu_1{}^2(s,\rho)$

$\mu_2(s,\rho) = \frac{\sum_{u \in A_2} I_j(u)}{N_2}$, $\sigma_2{}^2(s,\rho) = \frac{\sum_{u \in A_2} I_j{}^2(u)}{N_2} - \mu_2{}^2(s,\rho)$

we obtain $B(s,\rho)$ the Bhattacharyya distance [20], [18] between the distributions of the pixels contained A_1 and those contained inA_2:

$$B(s,\rho) = \frac{1}{4}(\mu_1(s,\rho) - \mu_2(s,\rho))^2 \sqrt{\sigma_1{}^2(s,\rho) + \sigma_2{}^2(s,\rho)} - \frac{1}{2} log(\frac{2\sigma_1(s,\rho)\sigma_2(s,\rho)}{\sigma_1{}^2(s,\rho) + \sigma_2{}^2(s,\rho)}) \quad (3)$$

Recall that Λ_S consists of components of $\mathcal{S}_{Th,j}$ with at most one m_c. For a λ with no pixel determined as m_c, the X and Y coordinates of m_c are approximated by rounding the means of the X-coordinates of the set of $\{m_{c,x}\}$ and the Y-coordinates of the set of $\{m_{c,y}\}$, respectively. Next, as shown in Figure 2 (b), a pixel $s_a \in \lambda$ that is farthest (in Euclidean distance) from m_c is obtained. The vector from m_c to s_a is considered the semi-major axis, and a is considered to be the length of the vector. The orientation θ is now the angle that the vector from m_c to s_a subtends with the horizontal axis. A vector that is perpendicular to the semi-major axis is drawn from m_c within λ and b is determined to be the length to the farthest pixel along that vector. Next, a rectangular pixel window $W_{c,\lambda}$ of size $(w_c \times w_c)$ centered at m_c is further examined for other candidates for the object center, and a corresponding parameter space, $\mathcal{P}_\lambda = [a \pm w_a] \times [b \pm w_b] \times [\theta \pm w_\theta]$ is formed by varying a, b and θ. The center candidate and parameters from $W_c \times (\mathcal{P}_\lambda \cap \mathcal{P})$ that maximize $B(s,\rho)$, are chosen as the ellipse center c_λ with parameters ρ_λ for λ, that is

$$(c_\lambda, \rho_\lambda) = \underset{s \in W_c, \rho \in \mathcal{P}_\lambda \cap \mathcal{P}}{\arg\max} B(s,\rho)$$

where $\mathcal{P}$ is the parameter space defined for our object model. An object centered at c_λ with parameters ρ_λ is thus generated.

Marked Point Process: We employ a marked point process approach based on the spatial birth-death process described in [18]. In our method, an object can be generated only when its center pixel belongs to Λ_M. Let Γ be the configuration of objects with their corresponding parameters. $\Gamma = (\Gamma_s, \Gamma_\rho)$, where Γ_s is a set of pixels that are object centers and Γ_ρ is a set of their respective parameters. Let $H(\Gamma)$ be the energy function for the Gibbs distribution function for the configuration Γ during the spatial birth-death process simulation. Let $H_{\text{Object}}(s,\rho)$ be the term representing how well the object centered at s with parameters ρ fits the image data I_j:

$$H_{\text{Object}}(s,\rho) = \begin{cases} \frac{1-B(s,\rho)}{T} & \text{if } B(s,\rho) \geq T \\ e^{-\frac{B(s,\rho)-T}{3B(s,\rho)}} - 1 & \text{if } B(s,\rho) < T \end{cases}$$

where $B(s,\rho)$ is distance measure described in Equation 3 and T is a threshold. Let $H_{\text{Brightness}}(s)$ be the term accounting for the local brightness in the neighborhood of s in an image. $H_{\text{Brightness}}(s) = \tau_s$, where τ_s is the local mean for pixel s and was used in adaptive thresholding. We define birth energy $H_B(s,\rho)$ and birth rate $b(s,\rho)$ at pixel s for parameter set ρ as:

$$H_B(s,\rho) = H_{\text{Object}}(s,\rho) + H_{\text{Brightness}}(s),$$

$$b(s,\rho) = 1 + 9\frac{\max(H_B(s,\rho)) - H_B(s,\rho)}{\max(H_B(s,\rho) - \min(H_B(s,\rho)}$$

Let $b_c(s)$ be the cumulative birth rate and $b_n(s)$ be the normalized birth rate at pixel s:

$$b_c(s) = \sum_{\rho \in \mathcal{P}} b(s,\rho) \ , \ b_n(s) = \frac{b_c(s)}{\max_{s \in \Lambda_M} b_c(s)}$$

Let $H_{\text{Inter}}(s_1, s_2)$ be the energy term corresponding to the object interaction model that accounts for the closeness or overlap between the two objects centered at s_1 and s_2. It is determined based on the Euclidean distance between the centers:

$$H_{\text{Overlap}}(s_1, s_2) = \max(0, 1 - \frac{\|s_1, s_2\|}{2r})$$

Let $H_{\text{Peak}}(s)$ be the energy term representing the local maxima of the cumulative birth rate function. In case of object overlap, this term causes objects not centered at the peaks of the birth rate function to be more prone to being eliminated than the ones centered at the peaks. The local maxima pixels are also used for configuration initialization.

$$H_{\text{Peak}}(s) = \begin{cases} -h_P & \text{if } \sum_{\rho \in \mathcal{P}} b_c(s) \text{ has a local maxima at } s. \\ 0 & \text{Otherwise} \end{cases}$$

where h_P is a positive contant. Therefore the energy function is obtained as:

$$H(\Gamma) = \alpha\{ \sum_{(s,\rho)\in\Gamma} H_{\text{Object}}(s,\rho) + \sum_{s\in\Gamma_s} H_{\text{Brightness}}(s)\} + \sum_{s_1,s_2\in\Gamma_s} H_{\text{Overlap}}(s_1,s_2) + \sum_{s\in\Gamma_s} H_{\text{Peak}}(s)$$

where α is a positive constant. Now, a multiple birth-death process is simulated to optimize the energy function according to [18]:

1) Determine $H_{\text{Object}}(s,\rho)$, $H_{\text{Brightness}}(s)$, $H_B(s,\rho)$, $b(s,\rho)$, $b_c(s)$, $b_n(s)$ and $H_{\text{Peak}}(s)$ for all $s \in \Lambda_M$ and $\rho \in \mathcal{P}$.
2) *Parameter Initialization:* Set the inverse temperature $\beta = \beta_0$ and the discretization step $\delta = \delta_0$.
3) *Configuration Initialization:* Start with $\Gamma = \Gamma^0$ such that ${\Gamma_s}^0$ contains objects centered at s where $b_c(s)$ achieves local maxima and Γ_ρ) contains their parameters $argmax_{\rho\in\mathcal{P}} b(s,\rho)$ for each s respectively.
4) *Birth Step:* For each $s \in \Lambda_M$, if $s \notin \Gamma_s$ add a point at s with probability $\delta b_n(s)$ and give birth to an object of parameter ρ with probability $= \frac{b(s,\rho)}{\sum_{\rho\in\mathcal{P}} b(s,\rho)}$.
5) *Death Step:* Sort the configuration of points Γ from highest to lowest values of $H_B(s,\rho)$. For each sorted point s obtain death rate $d(s,\rho) = \frac{\delta a(s)}{1+\delta a(s)}$, where $a(s) = e^{-\beta(H(\Gamma/\{s,\rho\})-H(\Gamma))}$ and kill the object with probability $d(s)$.
6) *Convergence Test:* If all the objects born in the *Birth Step* are killed in the *Death Step*, stop. Otherwise, increase β and decrease δ by a geometric scheme using the common ratios Δ_β and Δ_δ respectively and go back to the *Birth Step*.

The proposed nuclei segmentation method is described next:

Our Proposed Segmentation Method

Require: Original image volume
Extract blue color-channel from the volume to obtain a grayscale stack $\mathcal{I}$ with images I_j, $j = 1, 2, ...J$
Do **Adaptive Thresholding** to $\mathcal{I}$ to get $\mathcal{S}_{Th}$
for Each image I_j **do**
  Obtain $\mathcal{S}_{Th,j}$ as segmentation mask for image j from $\mathcal{S}_{Th}$
  Use **Object Model** as ellipse with a_{min}, a_{max}, b_{min}, b_{max} and Δ_θ
  Do **Midpoint Analysis** to obtain Λ_S and Λ_M
  for Each component $\lambda \in \Lambda_S$ **do**
    Shape-Fitting by Distance Function Optimization with $m_{c,i}$'s, w_c, w_a, w_b, w_θ to produce $(c_\lambda, \rho_\lambda)$
  Do **Marked Point Process** using I_j, Λ_M, α, β_0, δ_0, Δ_β, Δ_δ, h_P, r and T to produce Ω_M
  Combine using *OR* operation Ω_S and Ω_M to produce final segmentation result Ω

III. EXPERIMENTAL RESULTS

We tested our method using images from three datasets taken from fluorescence microscopy of a rat kidney. The values used for the various parameters were $w_{Th,x} = w_{Th,y} = 15$, $w_{Th,z} = 3$, $w_{v,x} = w_{v,y} = 2$, $w_{v,z} = 1$ for adaptive thresholding, $\nu = 10$ pixels for midpoint analysis, and $w_a = w_b = 2$ and $w_\theta = 30^\circ$ for shape fitting, $\alpha = 0.5$, $\beta_0 = 0.5$, $\delta_0 = 0.5$, $\Delta_\beta = 1.05$, $\Delta_\delta = 0.95$, $h_P = 2$, $r = \frac{1}{2}(a_{\text{min}} + a_{\text{max}})$ and T as 1 percentile of $B(s,\rho)$, for marked point process. All parameters were selected without fine-tuning and kept unchanged for all datasets. It took between 70 and 110 MPP iterations for one image to converge to the final configuration. We tested 32 images from each dataset. Each image had three 8-bit color-channels. The details of our datasets with shape parameters are listed in Table I.

Table I: Details of the datasets with specific parameters

Dataset	**I**	**II**	**III**
Dimensions	512×512	640×640	512×512
τ_c	$10/255$	$5/255$	$10/255$
$(a_{\text{min}}, a_{\text{max}})$	$(4, 8)$	$(6, 14)$	$(4, 14)$
$(b_{\text{min}}, b_{\text{max}})$	$(2, 6)$	$(4, 12)$	$(2, 12)$
Δ_θ	30°	20°	30°

Figure 3 shows some examples of our segmentation results. In the bottom row, n indicates the count of cell nuclei segmented using elliptical disks from the original images shown in the top row. It can be observed that the original images from all datasets possess non-uniform brightness. *Dataset-II* contains a large completely dark region, whereas *Dataset-III* has smaller regions of darkness. Images, especially from *Dataset-I* and *Dataset-II*, contain labeling errors resulting in frequent appearances of bright regions not representing nuclei. In all cases, our proposed method segments most bright nuclei and many nuclei present in the darker regions of images were also segmented successfully. There were a few that were missed as well false detections as the shape parameters were not correctly obtained in those cases. Objective evaluation of our segmentation results proves to be difficult due to the lack of ground truth data, for which the true shape and position of each object in the volume is known [5]. In fact, ground truth is impossible to obtain in fluorescent microscopy, since both the shape and position of an object are fluid in living animals, and are inevitably altered in the process of isolating and fixing tissues. Overall, our method successfully segments nuclei, enabling their counting and shape characterization.

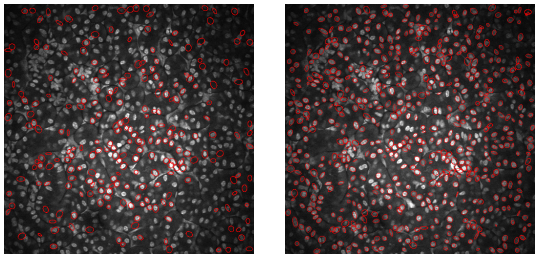

(a) Method from [18] ($n = 241$) (b) Our Method ($n = 628$)

Fig. 4: Comparison of the segmentation results. Outlines of segmented ellipse marks are represented by red and overlaid on the original image.

Figure 4 compares our method with the method described in [18] which we denote as $\mathcal{M}_{des}$. We used the object model and MPP parameters for $\mathcal{M}_{des}$ and our method. Note that $\mathcal{M}_{des}$ is applied directly on the original image without any preprocessing such as adaptive thresholding or midpoint analysis. Also, in $\mathcal{M}_{des}$ the energy term (H) consisted of the sum of only H_{Object} and H_{Inter}. Segmentation results (highlighted in red) from both methods are overlaid on the original images. Method $\mathcal{M}_{des}$ segments some nuclei at the center correctly. However, it failed to detect many nuclei from the less brighter regions , especially near the boundaries of the image. It also segmented many nuclei at places where there is no nucleus present visually. Our method provided a better segmentation detecting more nuclei correctly. In terms of computational time, our method takes on an average 20 times less than method $\mathcal{M}_{des}$ on the same machine. This is mainly because $\mathcal{M}_{des}$ computes the energy functions at every pixel of the image as against the selective MPP treatment performed in our method.

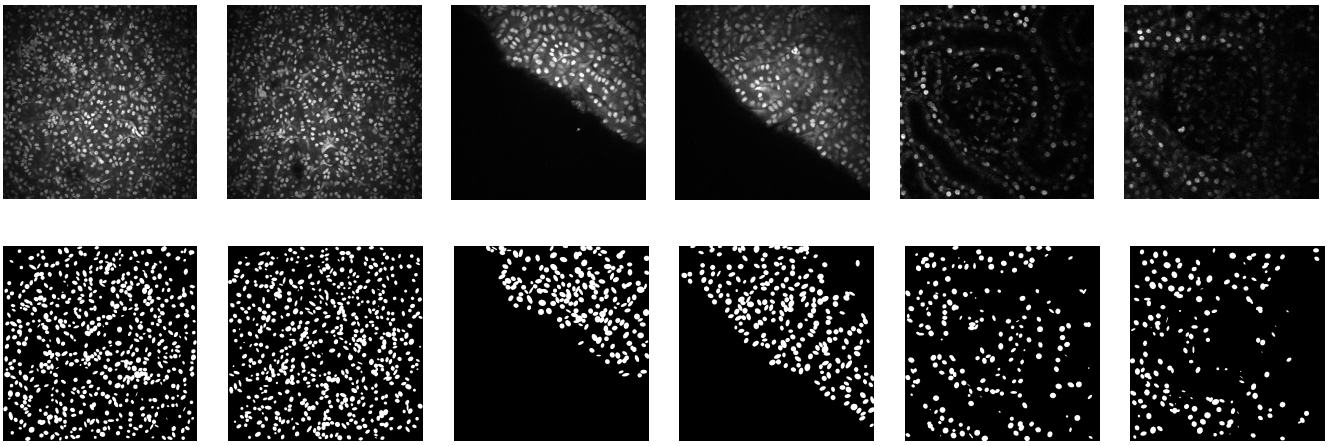

(a) n = 628 (b) n = 594 (c) n = 190 (d) n = 234 (e) n = 204 (f) n = 184

Fig. 3: Segmentation results of our proposed method (top row: original images, bottom row: segmentation results, columns 1-2: *Dataset-I*, columns 3-4: *Dataset-II* and columns 5-6 *Dataset-III*)

IV. CONCLUSIONS AND FUTURE WORK

In this paper we presented a method for segmentation of cell nuclei from fluorescence microscopy images of the kidney using midpoint analysis, shape-fitting and marked point process. Preliminary results obtained using various datasets of a rat kidney demonstrate that the proposed method is capable of counting cell nuclei and modeling them as individual objects with geometric shape parameters. In future, we plan develop an improved object interaction function with a 3D MPP approach. We also intend to incorporate differential geometry as an improvement to midpoint analysis.

V. REFERENCES

[1] M. Kyan, L. Guan, M. Arnison, and C. Cogswell, "Feature extraction of chromosomes from 3-D confocal microscope images," *IEEE Transactions on Biomedical Engineering*, vol. 48, no. 11, pp. 1306–1318, November 2001.

[2] K. Dunn, R. Sandoval, K. Kelly, P. Dagher, G. Tanner, S. Atkinson, R. Bacallao, and B. Molitoris, "Functional studies of the kidney of living animals using multicolor two-photon microscopy," *American Journal of Physiology-Cell Physiology*, vol. 283, no. 3, pp. C905–C916, September 2002.

[3] S. Ashworth, R. Sandoval, G. Tanner, and B. Molitoris, "Two-photon microscopy: Visualization of kidney dynamics," *Kidney International*, vol. 72, no. 4, pp. 416–421, May 2007, Nature Publishing Group.

[4] B. Luck, K. Carlson, A. Bovik, and R. Richards-Kortum, "An image model and segmentation algorithm for reflectance confocal images of in vivo cervical tissue," *IEEE Transactions on Image Processing*, vol. 14, no. 9, pp. 1265–1276, September 2005.

[5] K. Lorenz, P. Salama, K. Dunn, and E. J. Delp, "Three dimensional segmentation of fluorescence microscopy images using active surfaces," *Proceedings of the IEEE International Conference on Image Processing*, pp. 1153–1157, September 2013, Melbourne, Australia.

[6] C. Pluempitiwiriyawej, J. Moura, Y. Wu, and C. Ho, "STACS: New active contour scheme for cardiac MR image segmentation," *IEEE Transactions on Medical Imaging*, vol. 24, no. 5, pp. 593–603, May 2005.

[7] L. Coulot, H. Kirschner, A. Chebira, J. Moura, J. Kovacevic, E. Osuna, and R. Murphy, "Topology preserving STACS segmentation of protein subcellular location images," *Proceedings of the IEEE International Symposium on Biomedical Imaging*, pp. 566–569, April 2006, Arlington, VA.

[8] M. Velliste and R. Murphy, "Automated determination of protein subcellular locations from 3D fluorescence microscope images," *Proceedings of the IEEE International Symposium on Biomedical Imaging*, pp. 867–870, June 2002, Washington D.C.

[9] B. Matuszewski, M. Murphy, D. Burton, T. Marchant, C. Moore, A. Histace, and F. Precioso, "Segmentation of cellular structures in actin tagged fluorescence confocal microscopy images," *Proceedings of the IEEE International Conference on Image Processing*, pp. 3081–3084, September 2011, Brussels, Belgium.

[10] J. Cheng and J. Rajapakse, "Segmentation of clustered nuclei with shape markers and marking function," *IEEE Transactions on Biomedical Engineering*, vol. 56, no. 3, pp. 741–748, March 2009.

[11] L. Vincent and P. Soille, "Watersheds in digital spaces: an efficient algorithm based on immersion simulations," *IEEE Transactions on Pattern Analysis and Machine Intelligence*, vol. 13, no. 6, pp. 583–598, June 1991.

[12] X. Yang, H. Li, and X. Zhou, "Nuclei segmentation using marker-controlled watershed, tracking using mean-shift, and Kalman filter in time-lapse microscopy," *IEEE Transactions on Circuits and Systems-I: Regular Papers*, vol. 53, no. 11, pp. 2405–2414, November 2006.

[13] G. Srinivasa, M. Fickus, Y. Guo, A. Linstedt, and J. Kovacevic, "Active mask segmentation of fluorescence microscope images," *IEEE Transactions on Image Processing*, vol. 18, no. 8, pp. 1817–1829, August 2009.

[14] M. Plissiti and C. Nikou, "Overlapping cell nuclei segmentation using a spatially adaptive active physical model," *IEEE Transactions on Image Processing*, vol. 21, no. 11, pp. 4568–4580, November 2012.

[15] S. Arslan, T. Ersahin, R. Cetin-Atalay, and C. Gunduz-Demir, "Attributed relational graphs for cell nucleus segmentation in fluorescence microscopy images," *IEEE Transactions on Medical Imaging*, vol. 32, no. 6, pp. 1121–1131, June 2013.

[16] J. Bergeest and K. Rohr, "Segmentation of cell nuclei in 3D microscopy images based on level set deformable models and convex minimization," *Proceedings of the IEEE International Symposium on Biomedical Imaging*, pp. 637–640, April 2014, Beijing, China.

[17] M. Van Lieshout, *Markov point processes and their applications*. Imperial College Press, 2000, London, United Kingdom.

[18] X. Descombes, R. Minlos, and E. Zhizhina, "Object extraction using a stochastic birth-and-death dynamics in continuum," *Journal of Mathematical Imaging and Vision*, vol. 33, no. 3, pp. 347–359, March 2009.

[19] X. Descombes, F. Kruggel, G. Wollny, and H. Gertz, "An object-based approach for detecting small brain lesions: application to Virchow-Robin spaces," *IEEE Transactions on Medical Imaging*, vol. 23, no. 2, pp. 246–255, February 2004.

[20] H. Zhao, M. Comer, and M. De Graef, "A unified Markov random field/marked point process image model and its application to computational materials," *Proceedings of the IEEE International Conference on Image Processing*, p. To Appear, October 2014, Paris, France.

[21] C. Benedek and X. Descombes and J. Zerubia, "Building development monitoring in multitemporal remotely sensed image pairs with stochastic birth-death dynamics," *IEEE Transactions on Pattern Analysis and Machine Intelligence*, vol. 34, no. 1, pp. 33–50, January 2012.

[22] Q. Liao and Y. Deng, "An accurate segmentation method for white blood cell images," *Proceedings of the IEEE International Symposium on Biomedical Imaging*, pp. 245–248, June 2002, Washington D.C.